mathematics

MDPI

Article

Irreversibility Analysis in the Ethylene Glycol Based Hybrid Nanofluid Flow amongst Expanding/Contracting Walls When Quadratic Thermal Radiation and Arrhenius Activation Energy Are Significant

Bommana Lavanya [1,†], Jorige Girish Kumar [2], Macherla Jayachandra Babu [2], Chakravarthula Sivakrishnam Raju [3,4], Nehad Ali Shah [5,†] and Prem Junsawang [6,*]

[1] Department of Mathematics, Manipal Institute of Technology, Manipal Academy of Higher Education, Manipal 576104, Karnataka, India
[2] Department of Mathematics, S.V.A. Government College, Srikalahasti 517644, Andhra, India
[3] Department of Mathematics, GITAM School of Science, GITAM University, Bangalore Campus, Bangalore 562163, Karnataka, India
[4] School of Mechanical Engineering, Hanyang University, 222 Wangsimni-ro, Seongdong-gu, Seoul 04763, Korea
[5] Department of Mechanical Engineering, Sejong University, Seoul 05006, Korea
[6] Department of Statistics, Faculty of Science, Khon Kaen University, Khon Kaen 40002, Thailand
* Correspondence: prem@kku.ac.th
† These authors contributed equally to this work and are co-first authors.

check for updates

Citation: Lavanya, B.; Kumar, J.G.; Babu, M.J.; Raju, C.S.; Shah, N.A.; Junsawang, P. Irreversibility Analysis in the Ethylene Glycol Based Hybrid Nanofluid Flow amongst Expanding/Contracting Walls When Quadratic Thermal Radiation and Arrhenius Activation Energy Are Significant. *Mathematics* **2022**, *10*, 2984. https://doi.org/10.3390/math10162984

Academic Editor: Carlos Llopis-Albert

Received: 1 August 2022
Accepted: 16 August 2022
Published: 18 August 2022

Abstract: In this new era of the fluid field, researchers are interested in hybrid nanofluids because of their thermal properties and potential, which are better than those of nanofluids when it comes to increasing the rate at which heat is transferred. Compared to the dynamics of radiative Ethylene Glycol-Zinc Oxide (nanofluid) and Ethylene Glycol-Zinc Oxide-Titanium Dioxide (hybrid nanofluid) flows between two permeable expanding/contracting walls, nothing is known in terms of Lorentz force, heat source, and the activation energy. The thermo-physical characteristics of Ethylene Glycol, Zinc Oxide nanoparticles, and Titanium Dioxide nanoparticles are used in this study to derive the governing equations for the transport of both dynamics. Governing equations are converted as a set of nonlinear ordinary differential equations (with the aid of suitable similarity mutations), and then the MATLAB bvp4c solver is used to solve the equations. This study's significant findings are that rise in the reaction rate constant increases mass transfer rate, whereas an increase in the activation energy parameter decreases it. The mass transfer rate decreases at a rate of 0.04669 (in the case of hybrid nanofluid) and 0.04721 (in the case of nanofluid) when activation energy (E) takes input in the range $0 \leq E \leq 5$. It has been noticed that the velocity profiles are greater when the walls are expanding as opposed to when they are contracting. It is detected that the heat transfer rate reduces as the heat source parameter increases. The heat transfer rate drops at a rate of 0.9734 (in the case of hybrid Nanofluid) and 0.97925 (in the case of nanofluid) when the heat source parameter (Q) takes input in the range $0 \leq Q \leq 0.3$. In addition, it has been observed that the entropy generation increases as the Brinkmann number rises.

Keywords: quadratic thermal convection; expanding/contracting walls; entropy generation; bvp4c; quadratic thermal radiation; activation energy

MSC: 91G60

1. Introduction

Nanofluids, a novel type of heat transfer fluid, have been presented as an alternative to traditional fluids in industrial processes. Because of their modest size, erosion and corrosion are greatly reduced. Refrigeration, heat exchangers, and electronic device cooling are just a few of the many uses for nanofluids. In the beginning, Choi [1] discussed the pioneering work that was done on the flow dynamics of nanofluids. He came to the conclusion that the thermal conductivity of any fluid may be significantly improved by the addition of nanoparticles to the fluid. Moraveji and Toghraie [2] analyzed the effects of a number of inlets, tube length, and diameter of cold outlet on temperature and flow rates passing through the vortex tube. They concluded that the passing flow rate from a cold outlet is increased as its diameter increase. Kavusi and Toghraie [3] made a two-dimensional numerical model that uses different nanofluids to simulate how a heat pipe works. They saw that when a nanofluid is used instead of water, the thermal efficiency goes up and the heat at the wall of the heat pipe goes down. Mostafazadeh et al. [4] numerically investigated the effect of thermal radiation on the natural and steady convection of nanofluid in a vertical channel with the two-phase mixture and single-phase methods. It is noticed that the velocity is lower for the constant heat flux case compared with the constant temperature case. Thameem Basha et al. [5] scrutinized the Falkner-Skan flow of SWCNH/Diamond-Ethylene glycol nanofluid over the wedge, plate, and stagnation point with the influence of an induced magnetic field and nonlinear radiation. They noticed that the Diamond nanoparticles dominate the SWCNH nanoparticles in a fluid flow over the wedge, plate, and stagnation point. Recently, several researchers [6–9] examined various nanofluid flows over distinct geometries, including the flow TiO_2/H_2O over an exponential elongating sheet. In contrast to mono nanofluid, a hybrid nanofluid contains more than one particle. Because of this, hybrid fluids have better heat transfer properties than mono fluids. Among the many uses for these materials are solar collectors and military hardware. Balla et al. [10] numerically studied the enhancement of heat transfer for hybrid nanofluids flowing in a circular pipe with constant heat flux. They observed that the heat transfer coefficient of nanofluids is strongly dependent on the nanoparticles and increases with an increasing volume concentration of nanoparticles. Iqbal et al. [11] analyzed the effects of the stagnation-point flow of an electrically conducting hybrid nanofluid ($Al_2O_3 - Ag/H_2O$) towards a stretching surface with an induced magnetic field. Their results revealed the fact that the velocity profile and induced magnetic field are greater for nanofluid as compared to hybrid nanofluid. Mehran et al. [12] theoretically examined the free convective heat transfer of a hybrid nanofluid ($Cu - Al_2O_3/H_2O$) flow within a square porous cavity. They concluded that the reduction percentage of the heat transfer rate for a hybrid nanofluid is much more than that for a single regular nanofluid (Al_2O_3/H_2O). Mashayekhi et al. [13] studied the laminar flow of hybrid nanofluid ($Al_2O_3 - Cu/Water$) in a double-layered microchannel with sinusoidal walls. They discovered that increasing fluid viscosity increases shear stress, particularly at the wall and in fluid layers, and that this factor can enhance pressure drop in higher solid nanoparticle volume fractions. Ruhani et al. [14] developed a new model for the rheological behavior of Silica-Ethylene glycol/Water hybrid nanofluid. They discovered that, as the volume fraction increases, the relative viscosity increases due to the greater dispersion of the nanoparticles in the base fluid. Mabood et al. [15] discussed the entropy generation optimization in the hybrid nanofluid flow with the combined impacts of melting heat transfer and nonlinear thermal radiation. They discovered that as Eckert's number increases, so does Bejan's number and entropy generation. To study the radiative flow of Casson fluid mixed with a hybrid nanofluid (water + magnesium oxide + silver), Mousavi et al. [16] employed a heated extending sheet. As the suction parameter increases, the surface drag force increases, as well as one of their findings. Newly, a wide range of researchers [17–27] has examined several hybrid nanofluid flows with diverse parameters, including thermal radiation.

Some physical and biological conditions necessitate channels with walls that expand and compress. These include industrial cleaning chambers, aerospace engineering, filling machines, and coolant circulation. Researchers are interested in studying these fluxes because of the numerous uses they have. Research into the flow of water via channels with dilation/squeezing walls has yielded a variety of findings. Laminar and incompressible flow in a porous channel with expanding/contracting walls was studied by Zhou and Majdalani [28]. Raising the Reynolds number is observed to quicken flow turning and raise the axial to normal velocity ratio in injection-accelerated flows, according to the researchers' findings. The same channel was used by Raza et al. [29] to investigate the heat transfer characteristics of a nanofluid (Cu/H_2O) flow using a shooting approach. They found that when the volume proportion of nanoparticles increased, the fluid temperature decreased. Ahmed et al. [30] found that increasing the permeability of a nanofluid flow (Water + CNTs) in a channel with porous walls increased the rate of heat transfer at the top wall. In their study of the hybrid nanofluid ($H_2O/Cu - Al_2O_3$) flow, Saba et al. [31] discovered that the platelet shape conspicuously had greater temperature values as compared to brick and cylinder shapes of nanoparticles. The micropolar nature of the same hybrid nanofluid was explored by Mollamahdi et al. [32], who discovered that the micro rotation parameter declines with increased wall expansion. Ali et al. [33] studied the flow of nanofluid with Brownian motion and thermophoresis using HAM and discovered that the pressure gradient behavior is dependent on injection/suction with an increase in the deformation parameter. In recent studies, shah et al. [34] and Sajjan et al. [35] studied the thermal enhancement due to nanoparticles to investigate diverse nanofluid flows.

There is nothing known about comparing the dynamics of ethylene glycol-zinc oxide (nanofluid) and ethylene glycol-zinc oxide-titanium dioxide (hybrid nanofluid) flows between two permeable expanding/contracting walls when quadratic thermal radiation, magnetic field, and activation energy are important, after a thorough review of the literature. Irreversibility analysis is done in this study for the pertinent parameters, including the Brinkmann number. Engineering parameters of interest, such as mass transfer rate, are explained using graphs in this report.

2. Formulation

A laminar, two-dimensional, and Ethylene Glycol-Zinc Oxide-Titanium dioxide (hybrid nanofluid) flow through a permeable infinitely long rectangular channel with contracting/expanding walls (when quadratic thermal radiation, heat source, and activation energy are important) was studied in this work. Zno and TiO_2 were added to the base fluid (Ethylene Glycol) to create the hybrid nanofluid's composition. The x-axis goes in the same direction as the flow, while the y-axis goes in the opposite direction. The thermo-physical characteristics of this hybrid nanofluid are outlined in Table 1. When the channel dilates or contracts, the porous walls allow fluid to enter or depart, allowing the channel to expand or constrict. A time-dependent rate $\dot{a}(t) = \frac{da}{dt}$ is assumed to govern the expansion and contraction of the walls. The channel's initial height is $2a(t)$. In comparison to its breadth and length, the channel's height is considered to be extremely tiny in comparison. The flow geometry of the current problem is shown in Figure 1 below.

With these assumptions, equations which are governing the flow and boundary conditions are presented below (Sarojamma et al. [36], Al-Kouz et al. [37] and Irfan et al. [38]):

$$\frac{\partial u}{\partial x} + \frac{\partial v}{\partial y} = 0, \tag{1}$$

$$\begin{aligned} \frac{\partial u}{\partial t} + u\frac{\partial u}{\partial x} + v\frac{\partial u}{\partial y} &= -\frac{1}{\rho_{hnf}}\frac{\partial p}{\partial x} + \upsilon_{hnf}\left(\frac{\partial^2 u}{\partial x^2} + \frac{\partial^2 u}{\partial y^2}\right) \\ &+ g\Big(\beta_T(T - T_2) + \beta_{1T}(T - T_2)^2 + \beta_C(C - C_2)\Big) - u\frac{\sigma_{hnf}B_0^2}{\rho_{hnf}} \end{aligned} \tag{2}$$

$$(\rho C_p)_{hnf}\left(\frac{\partial T}{\partial t} + u\frac{\partial T}{\partial x} + v\frac{\partial T}{\partial y}\right) = k_{hnf}\left(\frac{\partial^2 T}{\partial x^2} + \frac{\partial^2 T}{\partial y^2}\right) - \frac{\partial q_R}{\partial y} + Q_0(T - T_2) \tag{3}$$

$$\frac{\partial C}{\partial t} + u\frac{\partial C}{\partial x} + v\frac{\partial C}{\partial y} = D_m\left(\frac{\partial^2 C}{\partial x^2} + \frac{\partial^2 C}{\partial y^2}\right) - k_r\left(\frac{T}{T_2}\right)^m \exp\left(-\frac{E_0}{k_1 T}\right)(C - C_2) \tag{4}$$

$$\left.\begin{array}{l} \text{at } y = -a \;:\; u = 0,\; v = -v_w = -A\dot{a},\; T = T_1,\; C = C_1 \\ \text{at } y = a \;\;\,:\; u = 0,\; v = v_w = A\dot{a},\quad T = T_2,\; C = C_2 \end{array}\right\} \tag{5}$$

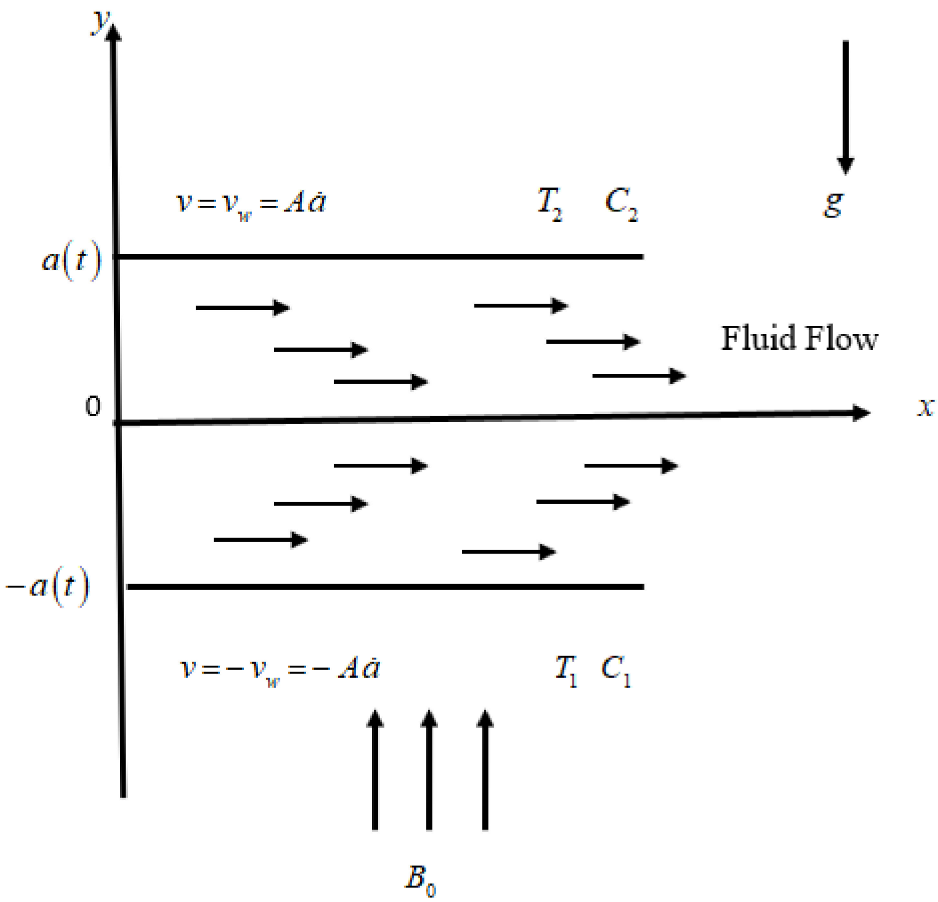

Figure 1. Flow diagram.

Table 1. Nanomaterial and base fluid's thermo-physical property values (Jamshed and Aziz [39]).

S. No.		Ethelene Glycol (EG)(f)	ZnO (s_1)	TiO_2 (s_2)
1	$\rho\left(\mathrm{kgm}^{-3}\right)$	1114	5660	4250
2	$C_p\left(\mathrm{J(kg\,K)}^{-1}\right)$	2415	495.2	686.2
3	$k\left(\mathrm{W(m\,K)}^{-1}\right)$	0.252	13	8.953
4	$\sigma\left(\mathrm{Sm}^{-1}\right)$	0.0000055	0.01	2,380,000

2.1. *Thermo-Physical Properties of Hybrid Nanofluid*

Heat capacity, viscosity, density, thermal conductivity, and electrical conductivity of the hybrid nanofluid are

$$\left.\begin{array}{l}(\rho C_p)_{hnf} = \left[(1-\phi_1)(\rho C_p)_f + \phi_1(\rho C_p)_{s_1}\right](1-\phi_2) + (\rho C_p)_{s_2}\phi_2, \\ \mu_{hnf} = \dfrac{\mu_f}{(1-\phi_1)^{2.5}(1-\phi_2)^{2.5}}, \rho_{hnf} = \left[(1-\phi_1)\rho_f + \phi_1\rho_{s_1}\right](1-\phi_2) + \rho_{s_2}\phi_2, \\ k_{hnf} = k_{nf} \times \dfrac{k_{s_2} + 2k_{nf} - 2k_{nf}\phi_2 + 2k_{s_2}\phi_2}{k_{s_2} + 2k_{nf} + k_{nf}\phi_2 - k_{s_2}\phi_2}, k_{nf} = k_f \times \dfrac{k_{s_1} + 2k_f - 2k_f\phi_1 + 2k_{s_1}\phi_1}{k_{s_1} + 2k_f + k_f\phi_1 - k_{s_1}\phi_1}, \\ \sigma_{hnf} = \sigma_{nf} \times \dfrac{\sigma_{s_2} + 2\sigma_{nf} - 2\sigma_{nf}\phi_2 + 2\sigma_{s_2}\phi_2}{\sigma_{s_2} + 2\sigma_{nf} + \sigma_{nf}\phi_2 - \sigma_{s_2}\phi_2}, \sigma_{nf} = \sigma_f \times \dfrac{\sigma_{s_1} + 2\sigma_f - 2\sigma_f\phi_1 + 2\sigma_{s_1}\phi_1}{\sigma_{s_1} + 2\sigma_f + \sigma_f\phi_1 - \sigma_{s_1}\phi_1}.\end{array}\right\}$$

In agreement with the theory by Al-Kouz et al. [37], the radiative heat flux q_R can be defined as

$$q_R = -\frac{4}{3k*}\frac{\partial}{\partial y}\left(\sigma * T^4\right) \tag{6}$$

With the aid of Taylor's series expansion T_∞ and by truncating the series after the second order term, we obtain

$$T^4 \approx T_\infty^4 + 4T_\infty^3(T - T_\infty) + 6T_\infty^2(T - T_\infty)^2 = 3T_\infty^4 - 8T_\infty^3 T + 6T_\infty^2 T^2 \tag{7}$$

Substituting Equation (7) into Equation (6) to obtain

$$q_R = \frac{-4\sigma*}{3k*}\frac{\partial}{\partial y}\left(3T_\infty^4 - 8T_\infty^3 T + 6T_\infty^2 T^2\right) \Rightarrow -\frac{\partial q_R}{\partial y} = -\frac{32\sigma * T_\infty^3}{3k*}\frac{\partial^2 T}{\partial y^2} + \frac{24\sigma * T_\infty^2}{3k*}\frac{\partial^2}{\partial y^2}(T)^2$$

With this, Equation (3) becomes,

$$(\rho C_p)_{hnf}\left(\frac{\partial T}{\partial t} + u\frac{\partial T}{\partial x} + v\frac{\partial T}{\partial y}\right) = k_{hnf}\left(\frac{\partial^2 T}{\partial x^2} + \frac{\partial^2 T}{\partial y^2}\right) - \frac{32\sigma * T_\infty^3}{3k*}\frac{\partial^2 T}{\partial y^2} + \frac{24\sigma * T_\infty^2}{3k*}\frac{\partial^2}{\partial y^2}(T)^2 + Q_0(T - T_2) \tag{8}$$

Variables for transformations proposed by Sarojamma et al. [36] are

$$\left.\eta = \frac{y}{a(t)},\ u = va^{-2}xF_\eta(\eta, t),\ v = -va^{-1}F(\eta, t),\ \theta = \frac{T - T_2}{T_1 - T_2},\ \Phi = \frac{C - C_2}{C_1 - C_2}\right\} \tag{9}$$

where $F_\eta = \frac{\partial F}{\partial \eta}$.

After eliminating the pressure term from (2) and applying (9), Equation (2), Equation (4), Equation (8) and boundary conditions in (5) changed as:

$$\frac{1}{H_1}F^{iv} + \alpha(3F'' + \eta F''') + \left(F'F'' - FF'''\right) - \frac{a^2}{v}\frac{\partial F''}{\partial t} - Gt\theta' - 2Gt\delta^*\theta\theta' - Gd\Phi' - \frac{H_3}{H_2}MF'' = 0 \tag{10}$$

$$\frac{1}{\Pr}\frac{1}{H_5}\left((H_4 + R + 3R\theta\theta_1 - 3R\theta)\theta'' + 3R(\theta_1 - 1)\theta'^2\right) + (\alpha\eta - F)\theta' - \frac{a^2}{v}\frac{\partial\theta}{\partial t} + \frac{1}{H_5}Q\theta = 0 \tag{11}$$

$$\frac{1}{Sc}\Phi'' + (\alpha\eta - F)\Phi' - \frac{a^2}{v}\frac{\partial\Phi}{\partial t} - \gamma(1 + \delta\theta)^m \exp\left(-\frac{E}{1 + \delta\theta}\right)\Phi = 0 \tag{12}$$

$$\left.\begin{array}{l}\text{at } \eta = -1 : \ F = -\mathrm{Re},\ F' = 0,\ \theta = 1,\ \Phi = 1 \\ \text{at } \eta = 1 \ \ : \ F = \mathrm{Re},\ \ F' = 0,\ \theta = 0,\ \Phi = 0\end{array}\right\} \tag{13}$$

Note that prime indicates the derivate w.r.t η.

Note that $\alpha = \frac{a\dot{a}}{v} > 0$ represents wall expansion, $\alpha < 0$ corresponds to wall contraction, Re is positive for suction and negative for injection.

One way to find a similar solution is to look at the case in which the non-dimensional parameter $\alpha(t) = \frac{a_0\dot{a}_0}{v}$ (a_0 and $\dot{a}_0$ denote the initial channel distance and expansion rate) F is a function of η, α instead of $\eta, tf = \frac{F}{\mathrm{Re}}$ (Dauenhauer and Majdalani [40]).

Then $f = f(\eta), \theta = \theta(\eta)$ and $\Phi = \Phi(\eta)$ which leads to $\frac{\partial f''}{\partial t} = \frac{\partial\theta}{\partial t} = \frac{\partial\Phi}{\partial t} = 0$.

With these changes, Equations (10)–(12) and the conditions (13) become:

$$\frac{1}{H_1}f^{iv} + \alpha(3f'' + \eta f''') + \left(f'f'' - ff'''\right) - \lambda\left((1 + 2\delta^*\theta)\theta' + \zeta\Phi'\right) - \frac{H_3}{H_2}Mf'' = 0 \tag{14}$$

$$(H_4 + R + 3R\theta\theta_1 - 3R\theta)\theta'' + H_5\Pr(\alpha\eta - \mathrm{Re}f)\theta' + 3R(\theta_1 - 1)\theta'^2 + \Pr Q\theta = 0 \tag{15}$$

$$\frac{1}{Sc}\Phi'' + (\alpha\eta - \mathrm{Re}f)\Phi' - \gamma(1 + \theta\delta)^m \exp\left(-\frac{E}{1 + \theta\delta}\right)\Phi = 0 \tag{16}$$

$$\left.\begin{array}{l}\text{at } \eta = -1 : \ f(\eta) = -1,\ f'(\eta) = 0,\ \theta(\eta) = 1,\ \Phi(\eta) = 1 \\ \text{at } \eta = 1 \ \ : \ f(\eta) = 1,\ \ f'(\eta) = 0,\ \theta(\eta) = 0,\ \Phi(\eta) = 0\end{array}\right\} \tag{17}$$

where

$$\left.\begin{array}{l}
H_1 = (1-\phi_2)\left[(1-\phi_1)+\phi_1\dfrac{\rho_1}{\rho_f}\right]+\phi_2\dfrac{\rho_2}{\rho_f}, H_2 = (1-\phi_1)^{2.5}(1-\phi_2)^{2.5},\\
H_{31} = \dfrac{\sigma_1+2\sigma_f-2\phi_1\left(\sigma_f-\sigma_1\right)}{\sigma_1+2\sigma_f+\phi_1\left(\sigma_f-\sigma_1\right)}, H_3 = \dfrac{\sigma_2+2H_{31}\sigma_f-2\phi_2\left(H_{31}\sigma_f-\sigma_2\right)}{\sigma_2+2H_{31}\sigma_f+\phi_2\left(H_{31}\sigma_f-\sigma_2\right)}H_{31},\\
H_{41} = \dfrac{k_1+2k_f-2\phi_1\left(k_f-k_1\right)}{k_1+2k_f+\phi_1\left(k_f-k_1\right)}, H_4 = \dfrac{k_2+2H_{41}k_f-2\phi_2\left(H_{41}k_f-k_2\right)}{k_2+2H_{41}k_f+\phi_2\left(H_{41}k_f-k_2\right)}H_{41},\\
H_5 = (1-\phi_2)\left[(1-\phi_1)+\phi_1\dfrac{(\rho C_p)_1}{(\rho C_p)_f}\right]+\phi_2\dfrac{(\rho C_p)_2}{(\rho C_p)_f},
\end{array}\right\}$$

and

$$\left.\begin{array}{c}
\alpha = \frac{a\dot{a}}{\upsilon}, M = \frac{\sigma B_0^2}{\mu a^{-2}}, \xi = \frac{x}{a}, Gt = \frac{g\beta_T(T_1-T_2)a^3}{\upsilon^2\xi}, Gd = \frac{g\beta_C(C_1-C_2)a^3}{\upsilon^2\xi},\\
\lambda = \frac{Gt}{\mathrm{Re}}, \zeta = \frac{Gd}{Gr}, R = \frac{16\sigma^* T_2^3}{3k_f k^*}, \theta_1 = \frac{T_1}{T_2}, \mathrm{Pr} = \frac{\mu C_p}{k_f}, \gamma = \frac{k_r a^2}{\upsilon}, \mathrm{Re} = \frac{Aa\dot{a}}{\upsilon} = \frac{av_w}{\upsilon},\\
Sc = \frac{\upsilon}{D_m},\ E = \frac{E_0}{k_1 T_2},\ \delta = \frac{T_1-T_2}{T_2},\ \delta^* = \frac{\beta_{1T}\Delta T}{\beta_T}.
\end{array}\right\}$$

2.2. Engineering Parameters of Concern

Skin friction coefficient near the lower wall is defined as:

$$C_{f_L} = \frac{\tau_w}{\rho v_w} \text{ where } \tau_w = \mu_{hnf}\left(\frac{\partial u}{\partial y}\right)_{y=-a} \tag{18}$$

With the help of (9), (18) can be rewritten as $(\mathrm{Re})C_{f_L} = \frac{1}{H_1}f''(-1)$.
Nusselt number and Sherwood numbers near the lower wall are defined as:

$$Nu_L = \frac{q_w}{\frac{k_f}{a}(T_1-T_2)},\ Sh_L = \frac{s_w}{\frac{D_m}{a}(C_1-C_2)}, \tag{19}$$

$$\text{where } q_w = -k_{hnf}\left(\frac{\partial T}{\partial y}\right)_{y=-a}, s_w = -D_m\left(\frac{\partial C}{\partial y}\right)_{y=-a} \tag{20}$$

By using (9) and (20), terms in (19) can be rewritten as

$$Nu_L = -H_4\theta'(-1), Sh_L = -\Phi'(-1)$$

Similarly, formulae to find the same parameters near the upper wall can be expressed as:

$$(\mathrm{Re})C_{f_U} = \frac{1}{H_1}f''(1), Nu_U = -H_4\theta'(1), Sh_U = -\Phi'(1)$$

2.3. Entropy Generation and Bejan Number

For a hybrid nanofluid flow between two porous walls (expanding/contracting), the formula to find the entropy generation is stated as follows:

$$\begin{aligned} S_G = {} & \tfrac{k_{hnf}}{T_2^2}\left[\left(\tfrac{\partial T}{\partial x}\right)^2+\left(\tfrac{\partial T}{\partial y}\right)^2\right]+\tfrac{\mu_{hnf}}{T_2}\left[2\left(\tfrac{\partial u}{\partial x}\right)^2+2\left(\tfrac{\partial v}{\partial y}\right)^2+\left(\tfrac{\partial u}{\partial y}+\tfrac{\partial v}{\partial x}\right)^2\right]+\tfrac{\sigma_{hnf}B_0^2}{T_2}u^2 \\ & +\tfrac{\overline{R}D_m}{C_2}\left(\tfrac{\partial C}{\partial y}\right)^2+\tfrac{\overline{R}D_m}{T_2}\left(\tfrac{\partial T}{\partial y}\right)\left(\tfrac{\partial C}{\partial y}\right) \end{aligned} \tag{21}$$

Equation (21), in its non-dimensional version, is

$$N_{EG} = H_4\delta\theta'^2 + \frac{H*}{H_1}\left(4BrF'^2 + Br_1F''^2\right) + H_3MBr_1F'^2 + H*\frac{\beta_0}{\delta}\Phi'^2 + H*\theta'\Phi' \quad (22)$$

With $f = \frac{F}{\mathrm{Re}}$ Equation (22) becomes

$$N_{EG} = H_4\delta\theta'^2 + \frac{H*\mathrm{Re}^2}{H_1}\left(4Brf'^2 + Br_1f''^2\right) + H_3MBr_1\mathrm{Re}^2f'^2 + H*\frac{\beta_0}{\delta}\Phi'^2 + H*\theta'\Phi' \quad (23)$$

Entropy generation parameter N_{EG}, Brinkmann number Br, Local Brinkmann number Br_1, diffusion parameter $H*$, and concentration ratio parameter β_0 are specified as:

$$\left.\begin{array}{c} N_{EG} = \frac{S_G a^2 T_2}{(T_1-T_2)k_f}, Br = \frac{\mu v^2}{a^2(T_1-T_2)k_f}, Br_1 = \frac{\mu v^2 x^2}{a^4(T_1-T_2)k_f}, H* = \frac{\overline{R}D_m(C_1-C_2)}{k_f}, \\ \beta_0 = \frac{C_1-C_2}{C_2}. \end{array}\right\}$$

The Bejan number may be calculated using the following expression:

$$Be = \frac{\text{Entropy production as a result of the transport of heat and mass}}{\text{The production of all entropy}}$$

By using (23), it is written as:

$$Be = \frac{H_4\delta\theta'^2 + H*\frac{\beta_0}{\delta}\Phi'^2 + H*\theta'\Phi'}{H_4\delta\theta'^2 + \frac{H*\mathrm{Re}^2}{H_1}\left(4Brf'^2 + Br_1f''^2\right) + H_3MBr_1\mathrm{Re}^2f'^2 + H*\frac{\beta_0}{\delta}\Phi'^2 + H*\theta'\Phi'}$$

3. Validation

An excellent match can be shown in Table 2, which shows comparisons between our results and those of previous studies.

Table 2. Comparison of the present results with those that have been previously reported $f''(1)$ under specific conditions, such as, $\phi_1 = \phi_2 = 0$.

M	Re	Bilal et al. [35]	Current Outcomes
0	0.5	4.713254	4.713217
1		4.739148	4.739109
2		4.820361	4.820342
3		4.396271	4.396280
2	0	1.842331	1.842323
	0.3	3.653601	3.653614
	0.6	5.391148	5.391142
	1	7.593006	7.593001

4. Discussion of Outcomes

Equations (14)–(16) together with the conditions (17) are solved with the help of bvp4c, MATLAB in-built function. The results are explained for two different types of nanofluids: nanofluid $(EG + ZnO)$ and hybrid nanofluid $(EG + ZnO + TiO_2)$. All results are established for the expansion case, i.e., $\alpha > 0$. The streamlines of the present hybrid nanofluid flow is presented in Figure 2. In this study, simulated the two cases of flow denoted as Solid Lines: Blue color: Hybrid Nanofluid and Dashed Lines: Red color: Nanofluid.

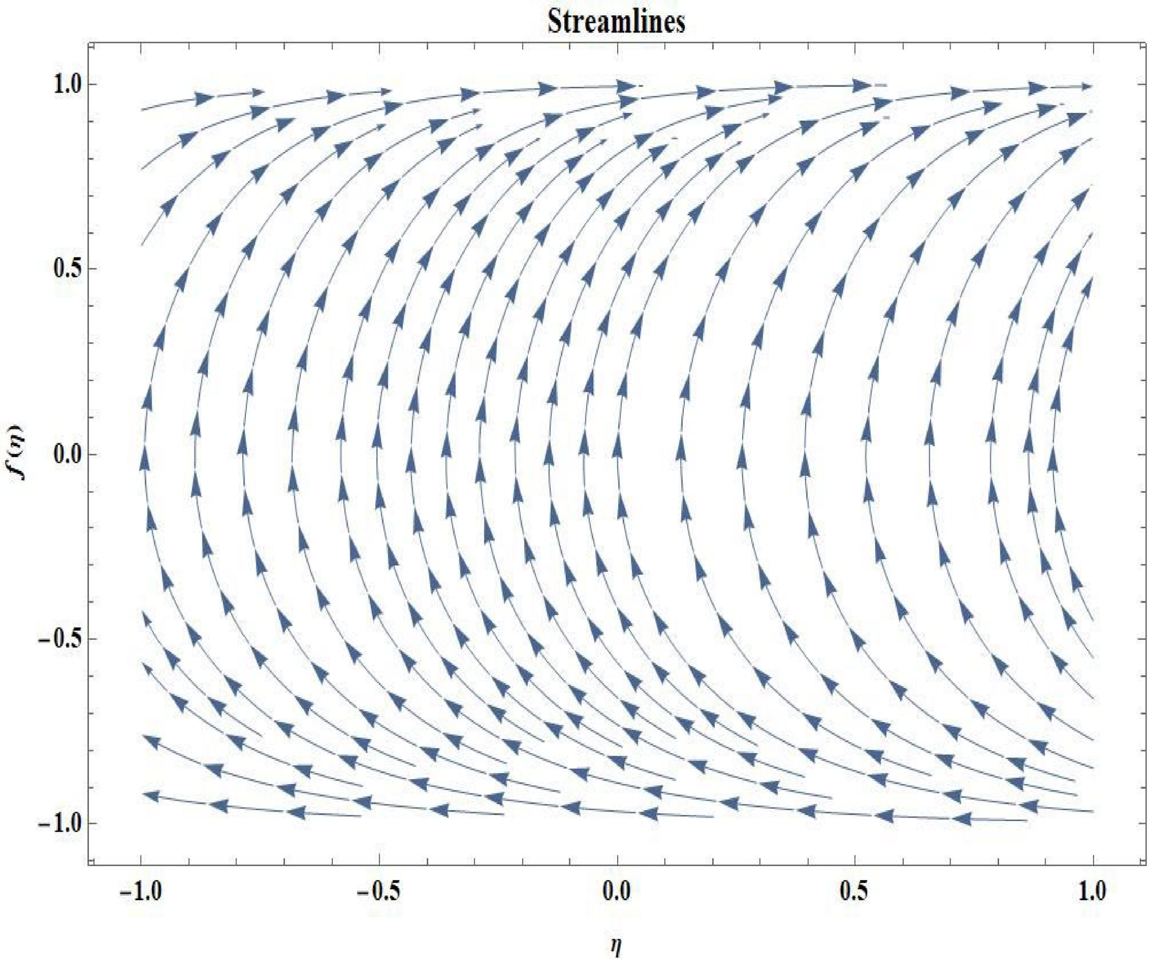

Figure 2. Streamlines of the present hybrid nanofluid flow.

4.1. Velocity Profiles

It is evident from Figure 3 that an increase in the suction parameter decreases the fluid velocity. In fact, strong suction attracts the heated fluid towards the boundary and increases the viscosity, which decelerates the fluid flow. Figure 4 exhibits the impact of the magnetic field on the velocity profile. It is discovered that the velocity diminishes with the rise in magnetic field parameters. Generally, the motion of the fluid is affected by an applied magnetic field. The particles of liquid structure chain turn towards the course of the applied attractive field. During this time, the particles are collided with one another, forming a barrier to the fluid flow. Fluid velocity decreases due to increased viscosity, as seen in Figure 4. Figure 5 shows that when walls contract, the velocity profiles are higher than when walls expand. This could be because of the space created by wall contraction/expansion. As the volume percentage of nanoparticles grows, the viscosity of the fluid increases, which impedes the flow. Consequently, the velocity decreases as the size ϕ_1 increases (see Figure 6).

4.2. Temperature Profiles

The heat energy of a fluid increases whenever it is exposed to a source of thermal radiation. As a result, temperature rises as thermal radiation rises (see Figure 7). These results are matched with Al-Kouz et al. [37], and Figure 8 depicts the effect of a heat source on a temperature profile. It can be seen that the temperature rises as the heat source increases. Increases in the heat source parameter typically result in an increase in the thermal boundary layer thickness of the fluid due to the propagation of excess heat.

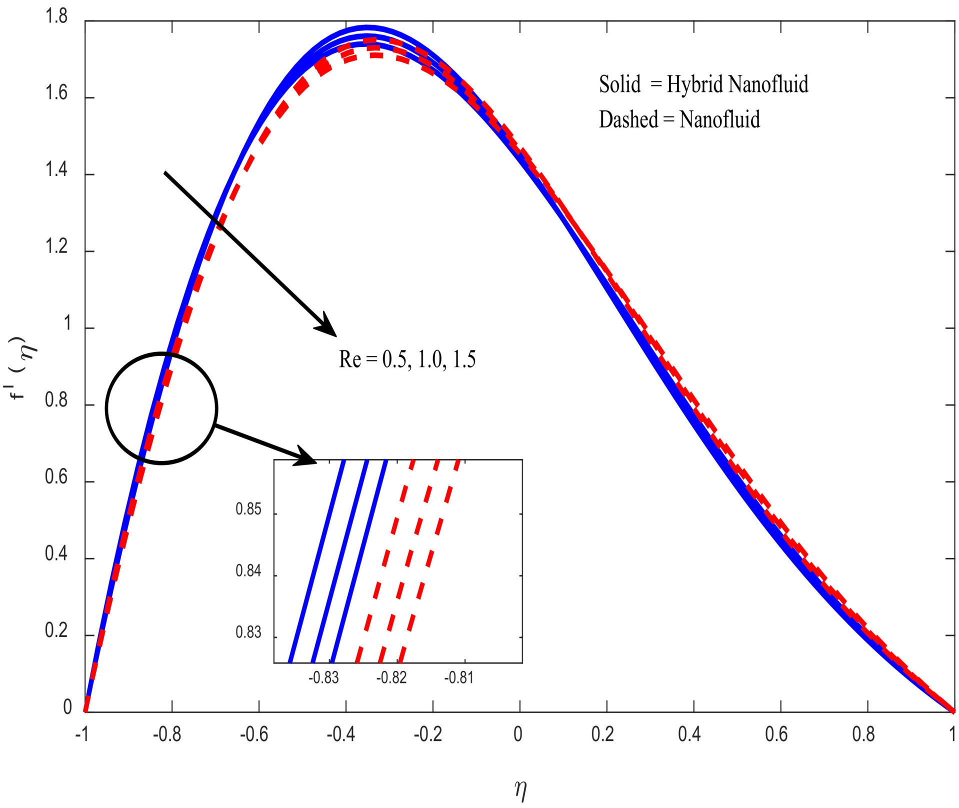

Figure 3. Influence of Re on the velocity profile.

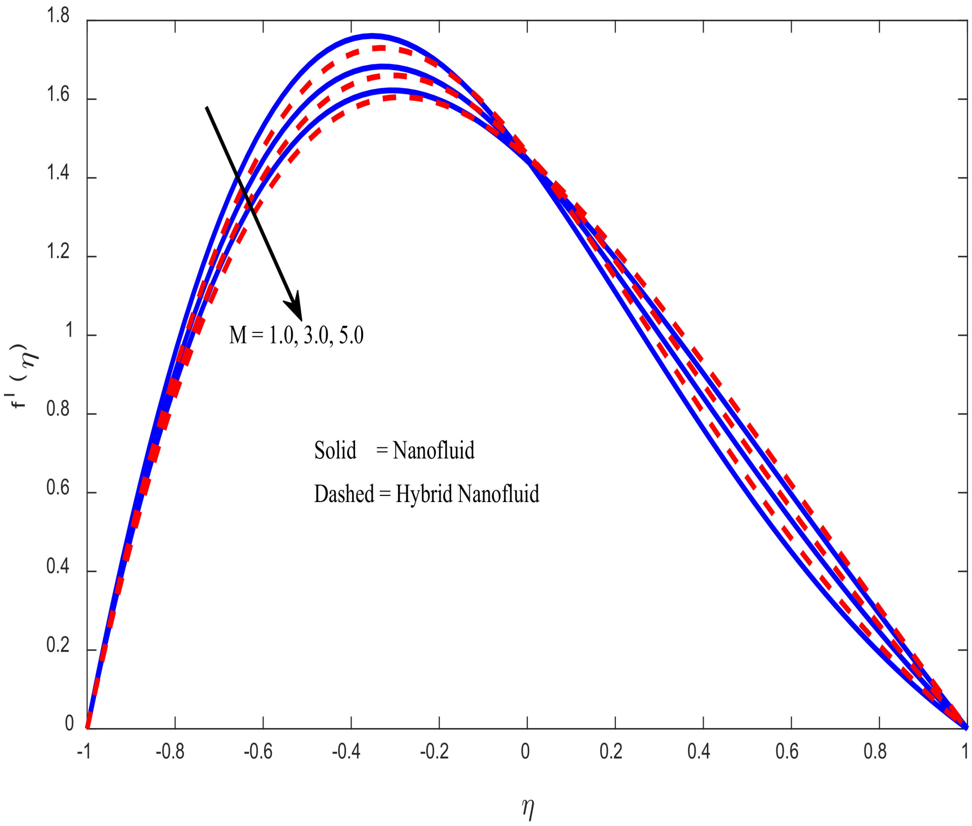

Figure 4. Influence of M on the velocity profile.

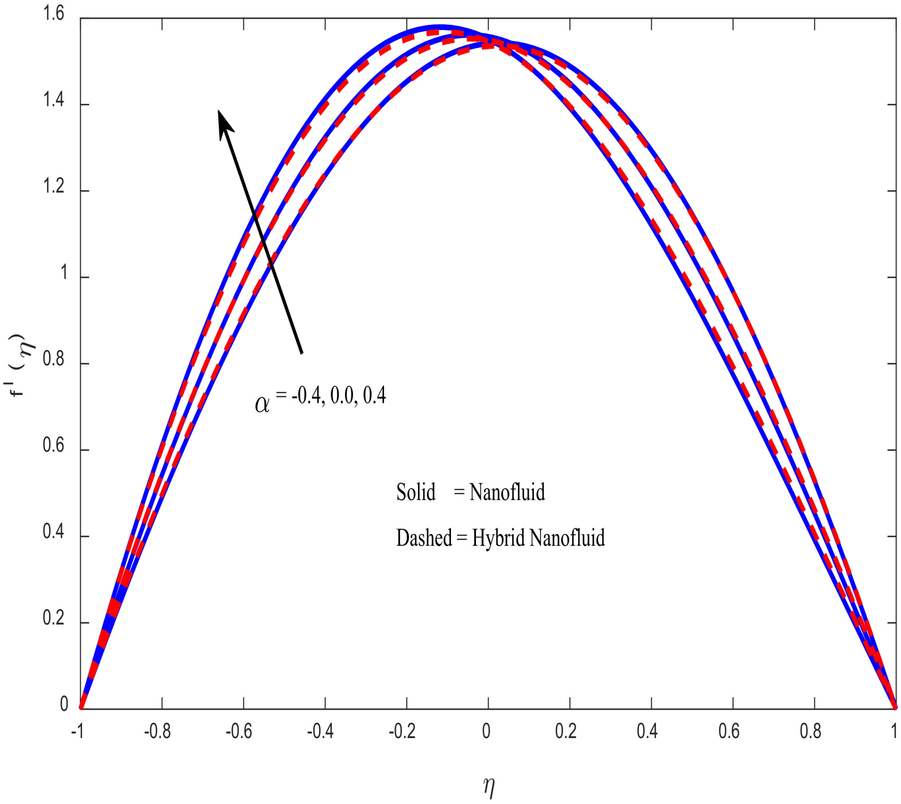

Figure 5. Influence of α on the velocity profile.

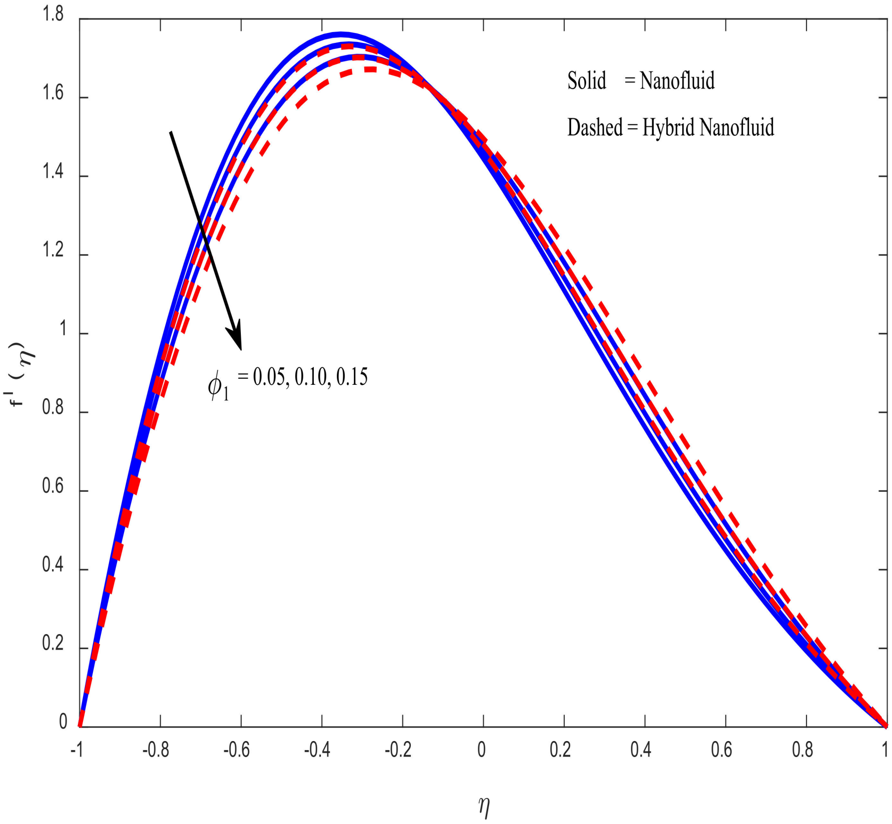

Figure 6. Influence of ϕ_1 on the velocity profile.

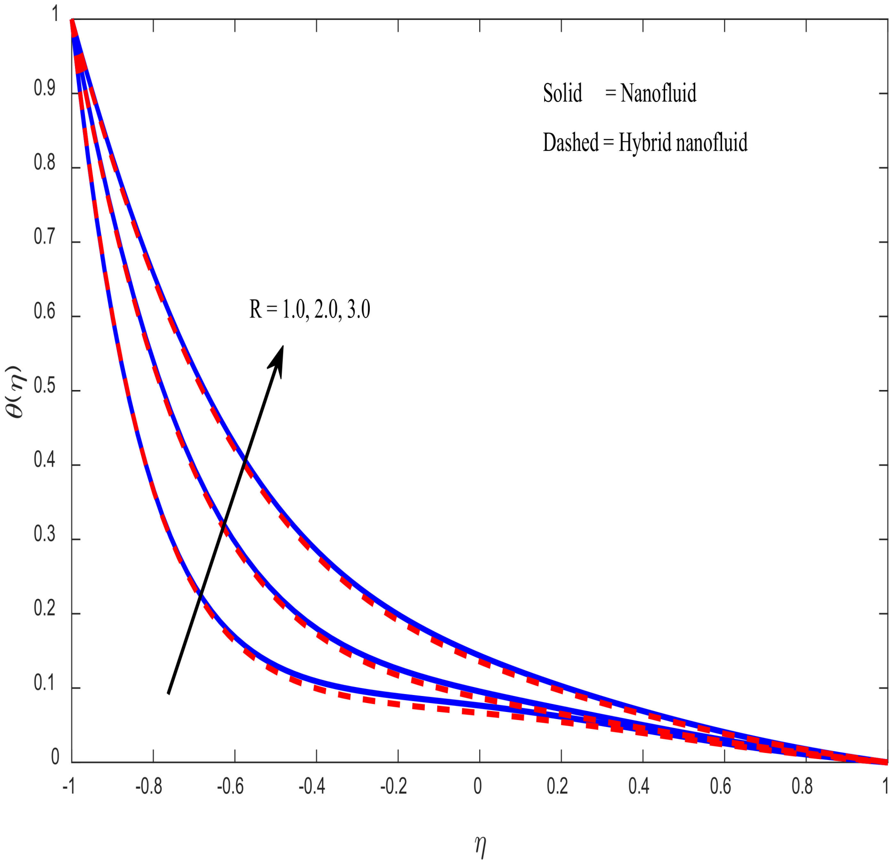

Figure 7. Influence of R on the temperature profile.

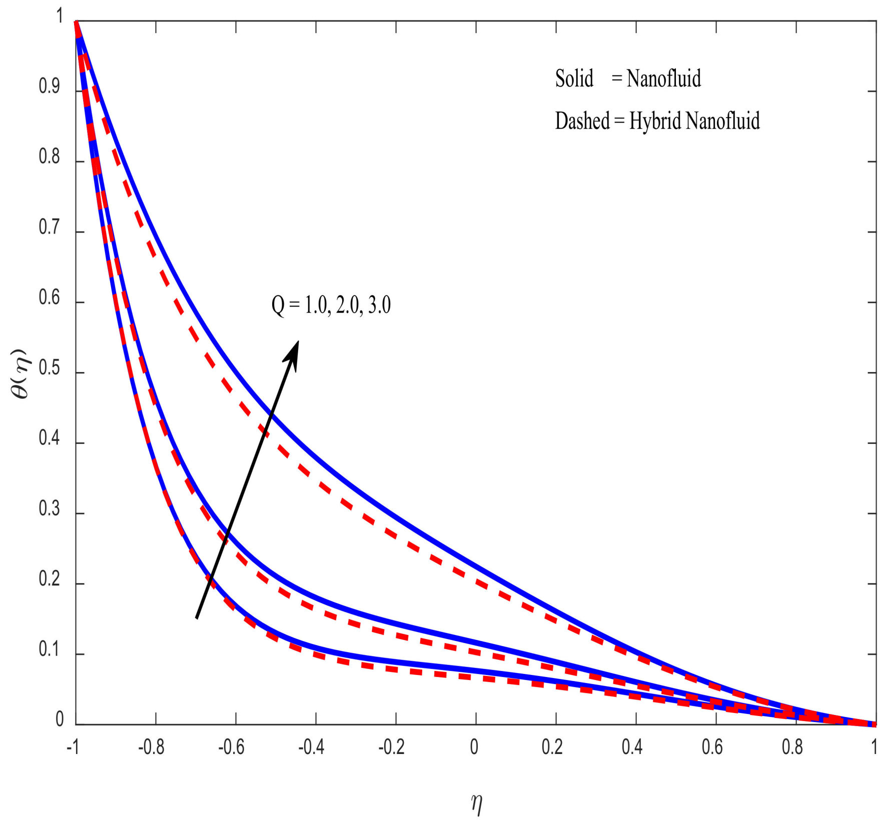

Figure 8. Influence of Q on the temperature profile.

4.3. Concentration Profiles

As depicted in Figure 9, raising the reaction rate decreases fluid concentration. This may be attributed to the production of high entropy. Figure 10 provides an explanation of the activation energy's effect on the concentration profile. As activation energy increases, fluid threshold energy decreases, influencing average kinetic energy. This circumstance demonstrates a lower average kinetic energy. As a result, the fluid will be more concentrated due to decreased diffusion.

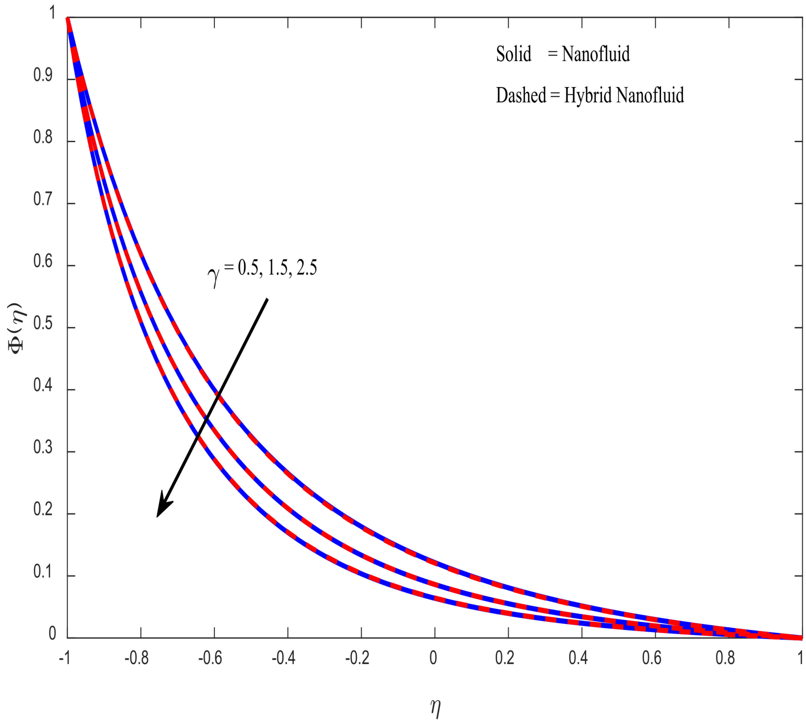

Figure 9. Influence of γ on the concentration profile.

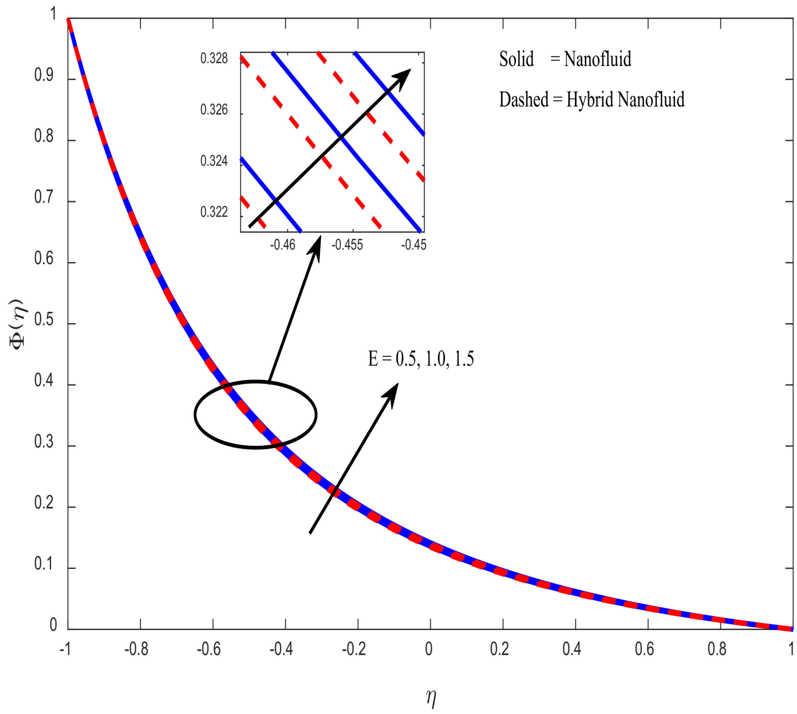

Figure 10. Influence of E on the concentration profile.

4.4. Engineering Parameters of Interest, Entropy Generation, and Bejan Number Profiles

Figures 11 and 12 show the effects of $M\phi_1$ and on the skin friction coefficient near the lower wall. Shear stress decreases with an increase in the magnetic field parameter. Consequently, there is a reduction in the skin friction coefficient (see Figure 11). It is noticed that when magnetic field parameter (M) takes an input in the range $0 \leq M \leq 3$, skin friction coefficient decreases at a rate of 0.10847 (in the case of hybrid nanofluid) and 0.13105 (in the case of nanofluid) per unit value of magnetic field parameter. As can be seen in Figure 12, the skin friction coefficient increases as ϕ_1 increases. With the increase in RQ, the heat transfer rate decreases as shown in Figures 13 and 14. Note that as the values of both parameters increase, the thermal conductivity of the fluid decreases. Since thermal conductivity and convective heat transfer coefficient are related, there is a decrease in the convective heat transfer coefficient. Consequently, the Nusselt number drops. The heat transfer rate drops at a rate of 0.9734 (in the case of hybrid Nanofluid) and 0.97925 (in the case of nanofluid) when the heat source parameter (Q) takes input in the range $0 \leq Q \leq 0.3$.

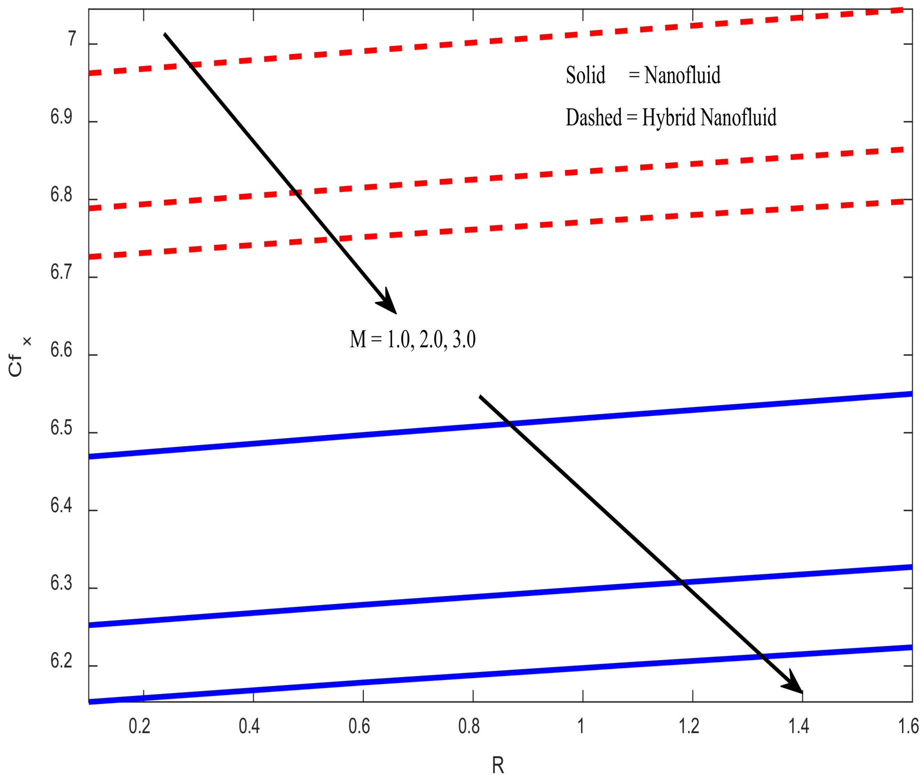

Figure 11. Influence of M on skin friction coefficient near the lower wall.

According to Figures 15 and 16, an increase in γ creases mass transfer rate, whereas an increase E decreases it. Note that as the activation energy parameter increase, the mass diffusivity of the fluid decreases. Since mass diffusivity and convective mass transfer coefficient are related, there is a decrease in the convective mass transfer coefficient. Consequently, the Sherwood number drops. Increasing the value γ results in a higher mass transfer rate, but increasing the value E has the opposite effect. The mass transfer rate decreases at a rate of 0.04669 (in the case of hybrid nanofluid) and 0.04721 (in the case of nanofluid) when activation energy (E) takes an input in the range $0 \leq E \leq 5$. It is observed that the same results are obtained near the upper wall. So, the results near the upper wall (C_{f_U}, Nu_U, Sh_U) are avoided in this report.

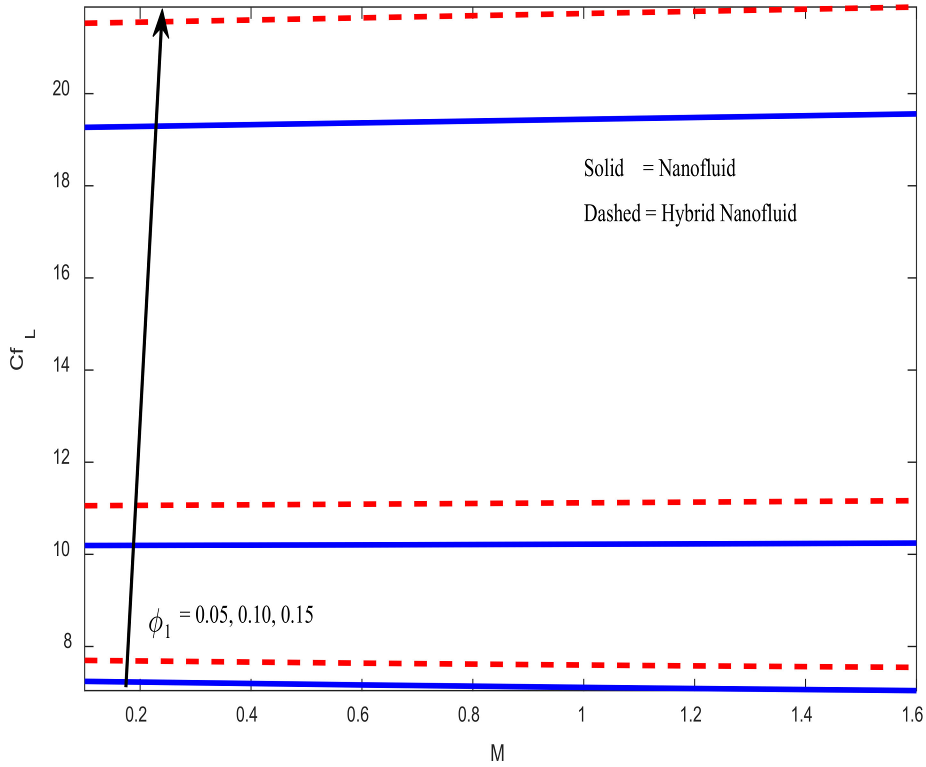

Figure 12. Influence of ϕ_1 on skin friction coefficient near the lower wall.

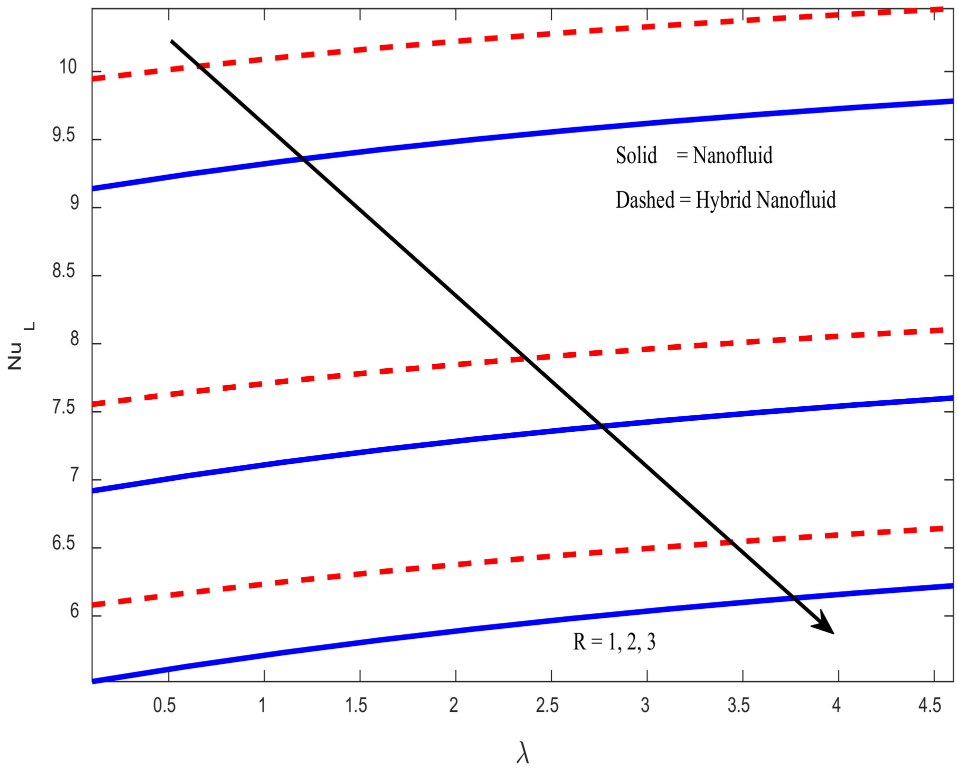

Figure 13. Influence of R on heat transfer rate near the lower wall.

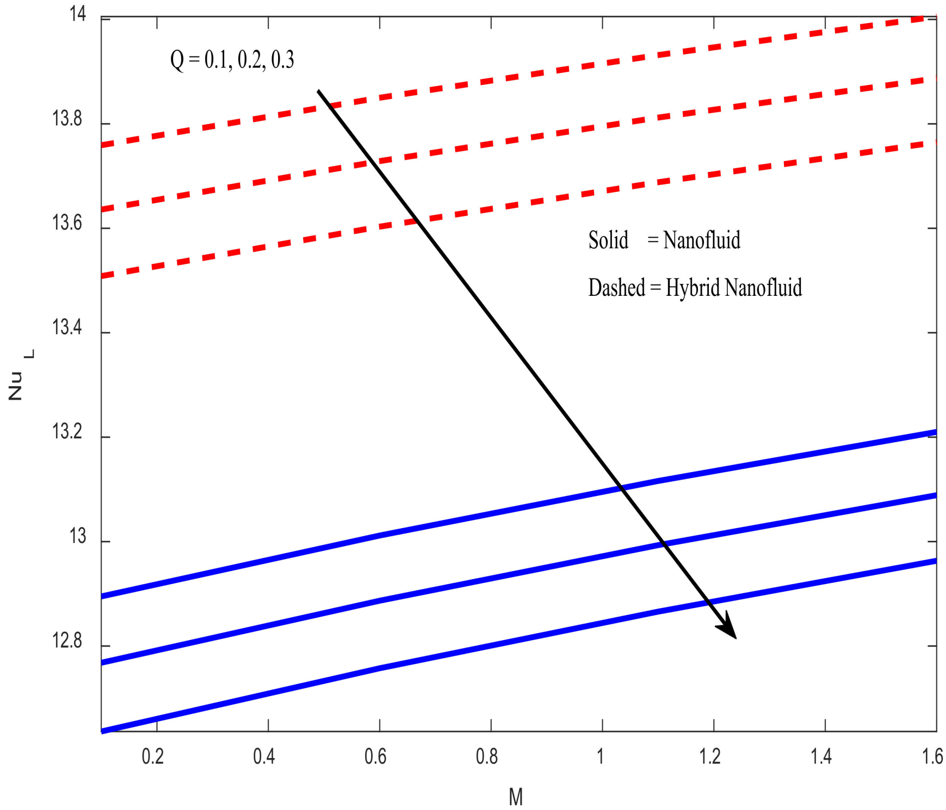

Figure 14. Influence of Q on heat transfer rate near the lower wall.

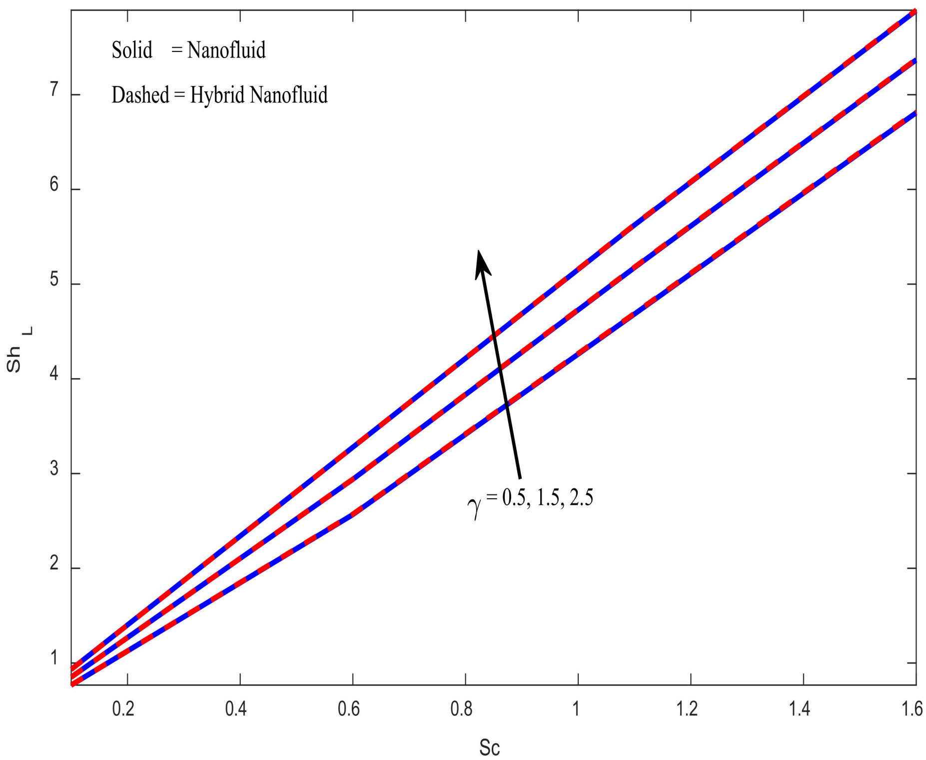

Figure 15. Influence of γ on Sherwood number near the lower wall.

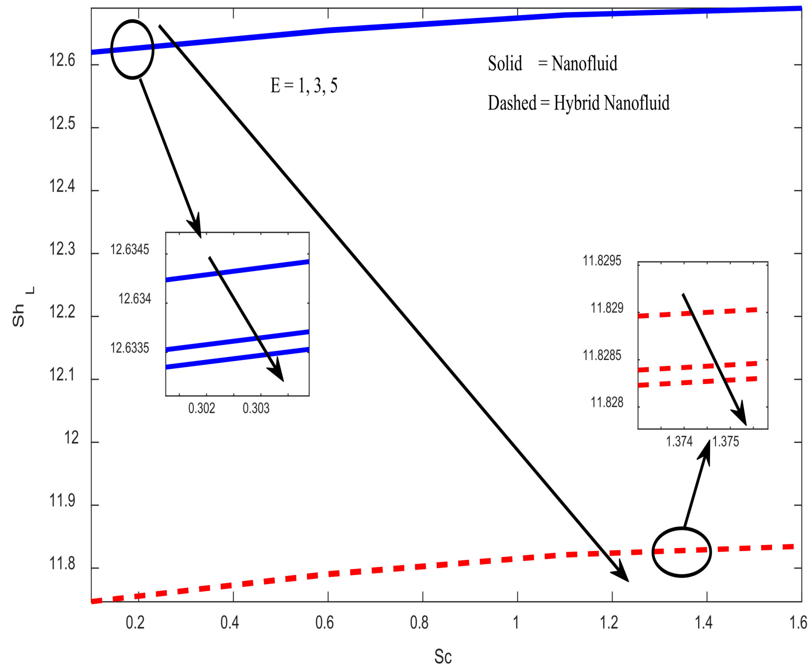

Figure 16. Influence of E on Sherwood number near the lower wall.

Figures 17–19 illustrate the impact of Br, M and ϕ_1 on the entropy generation profile. The rise in fluid viscosity resulting from an increase in Br causes an increase in entropy generation (see Figure 17). Entropy formation increases as M increases because the irreversibility of Joule dissipation increases as M rises (see Figure 18). As shown in Figure 19, a rise in ϕ_1 causes an increase in entropy generation. According to Figures 20–22, when the parameters $Br, M\phi_1$ rise, the Bejan number decreases. This may be due to the fact that the irreversibility of heat and mass transfer is eclipsed by the unchangeability of the other terms, including fluid friction.

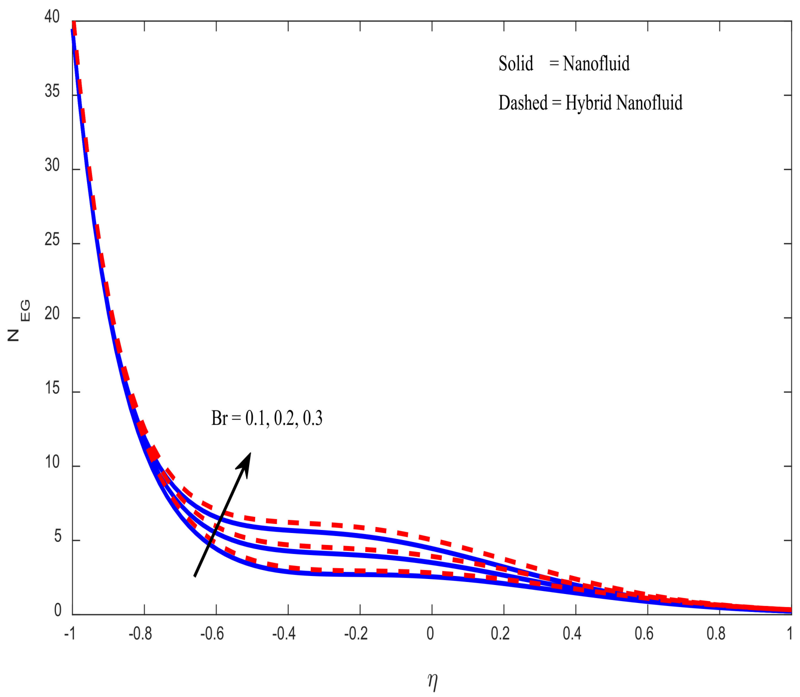

Figure 17. Influence of Br n entropy generation profile.

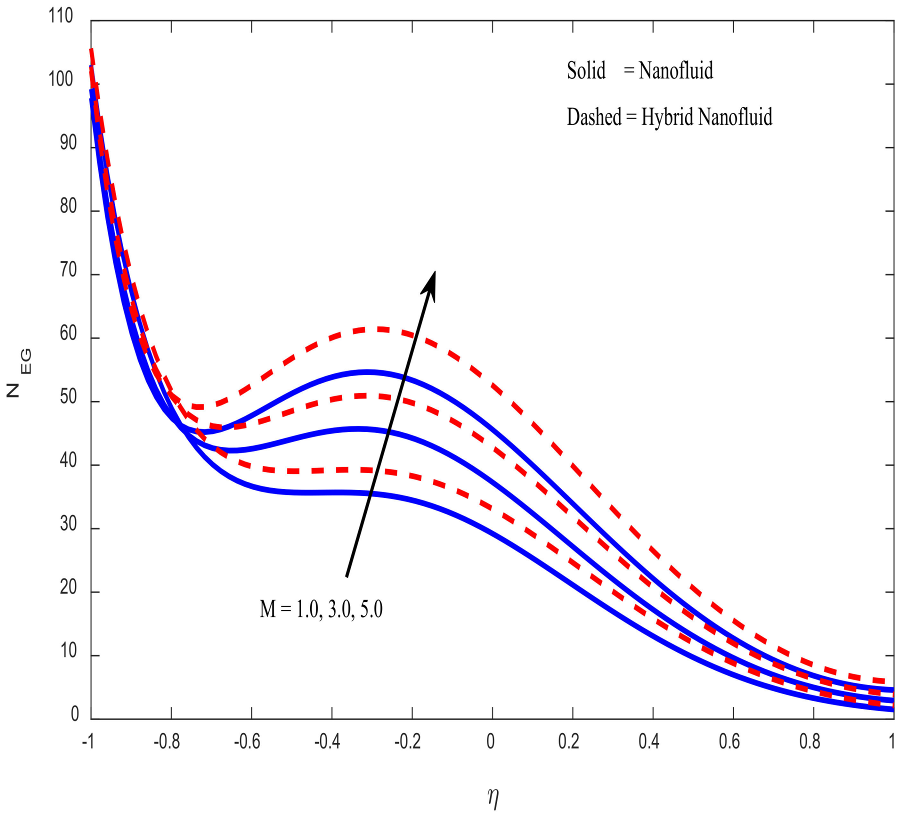

Figure 18. Influence of M on entropy generation profile.

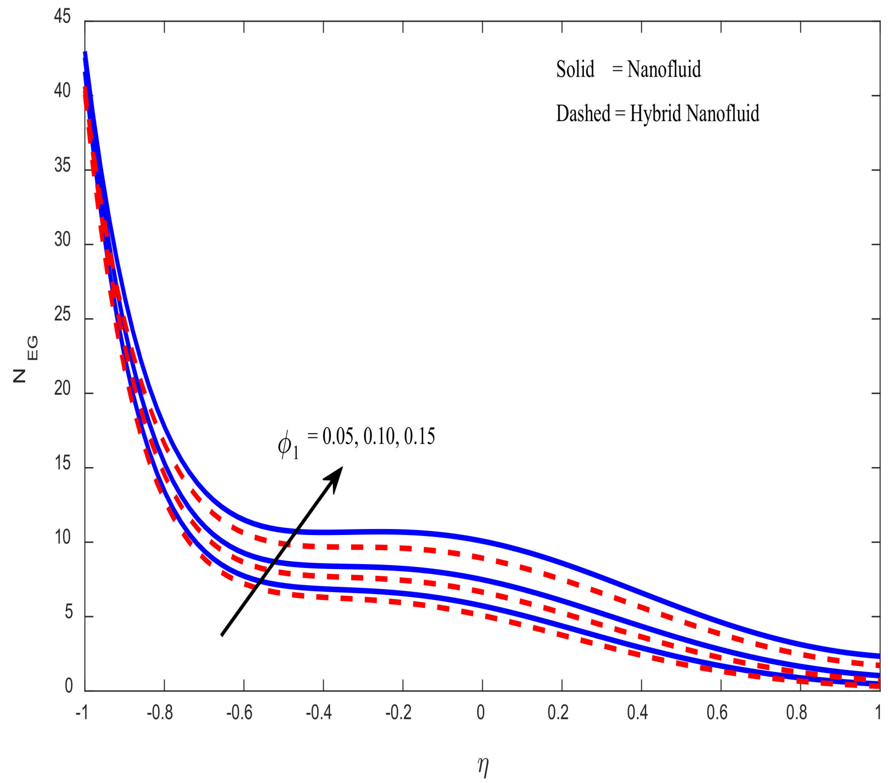

Figure 19. Influence of ϕ_1 on entropy generation profile.

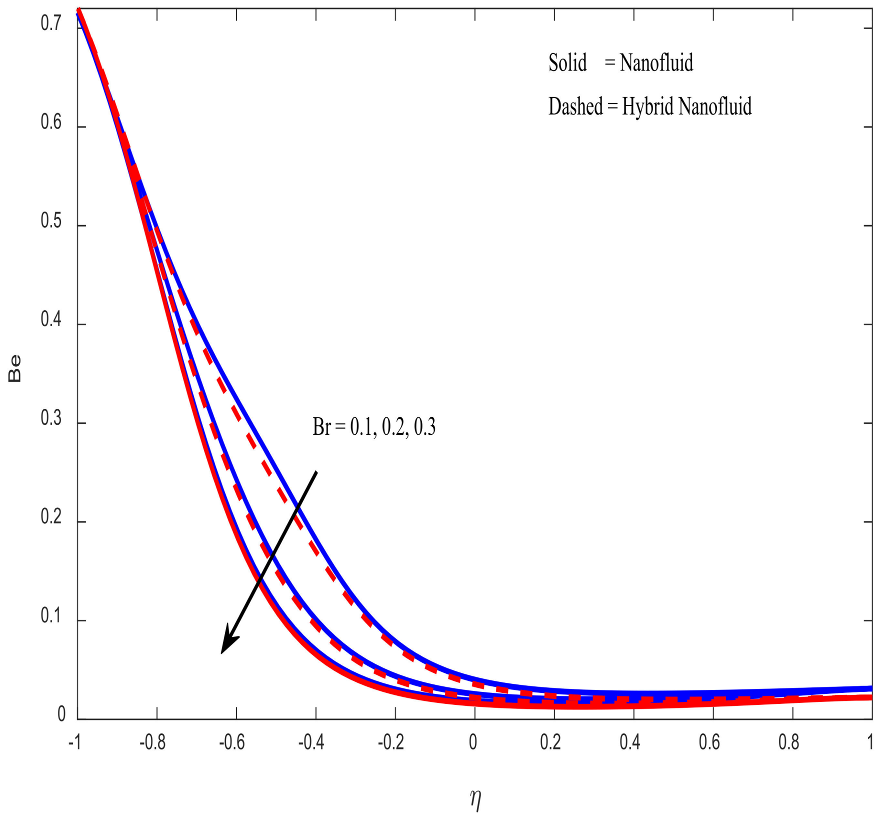

Figure 20. Influence *Br* on the Bejan number profile.

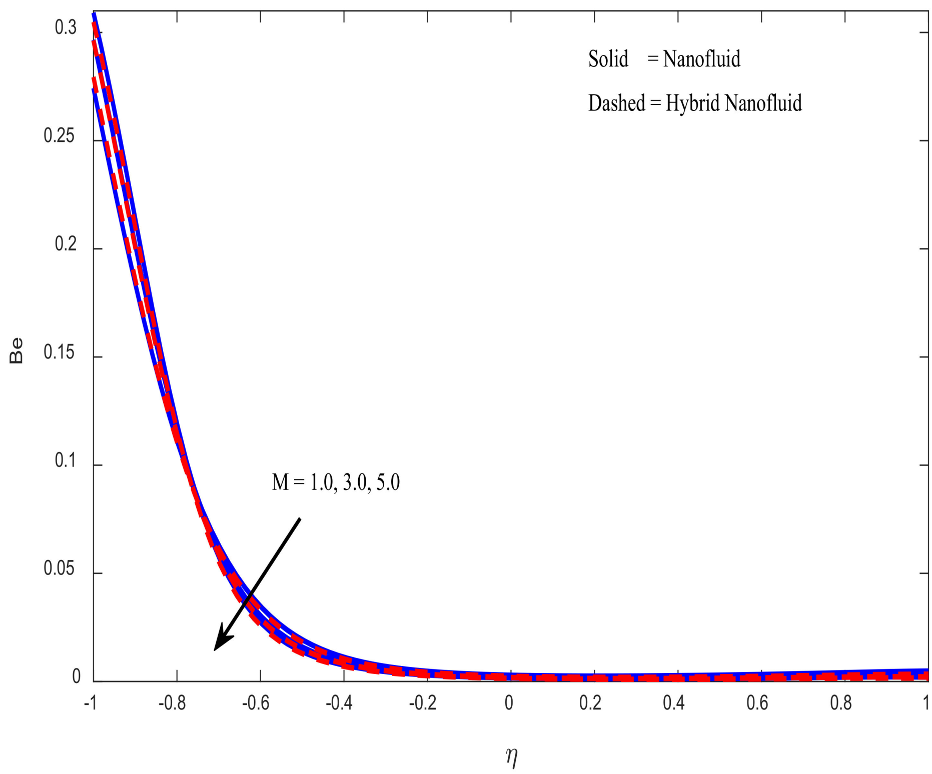

Figure 21. Influence of *M* on the Bejan number profile.

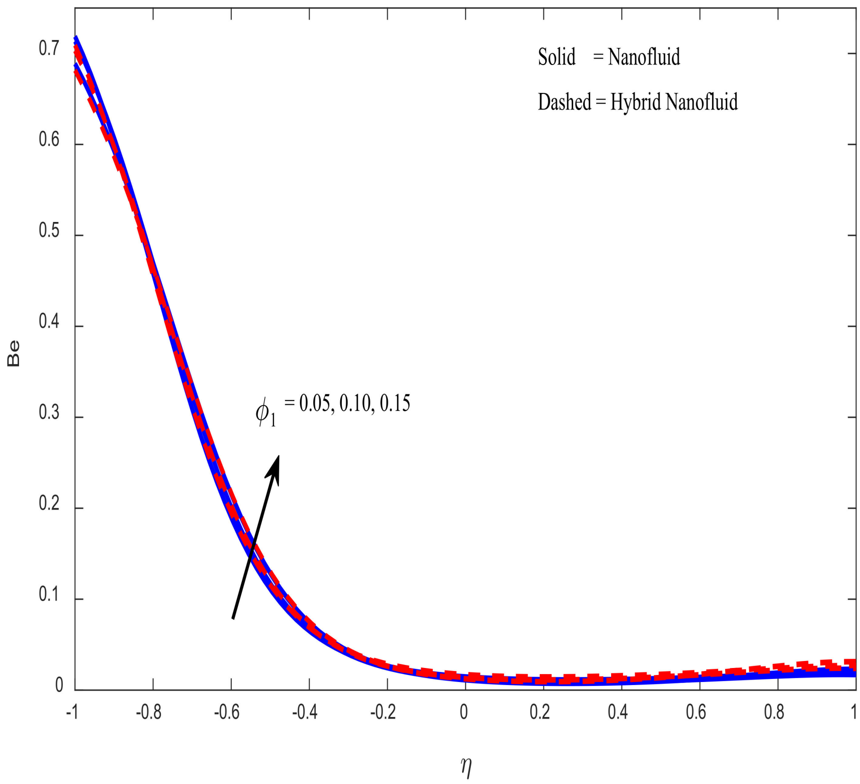

Figure 22. Influence of ϕ_1 on the Bejan number profile.

5. Conclusions

Ethylene Glycol-Zinc Oxide-Titanium dioxide (hybrid nanofluid) flow between two permeable expanding/contracting walls with the magnetic field parameter was investigated in this study when quadratic thermal radiation, heat source, and activation energy are important. Based on the analysis and discussion of the results, it is worthy to conclude that:

- As the magnetic field parameter increases, the skin friction coefficient decreases. It is noticed that, when magnetic field parameter (M) takes an input in the range $0 \leq M \leq 3$, skin friction coefficient decreases at a rate of 0.10847 (in the case of hybrid nanofluid) and 0.13105 (in the case of nanofluid) per unit value of magnetic field parameter.
- The rate of heat transfer reduces as the value of the heat source parameter increases. The heat transfer rate drops at a rate of 0.9734 (in the case of hybrid Nanofluid) and 0.97925 (in the case of nanofluid) when the heat source parameter (Q) takes an input in the range $0 \leq Q \leq 0.3$.
- Increasing the value of γ results in a higher mass transfer rate but increasing the value E has the opposite effect. The mass transfer rate decreases at a rate of 0.04669 (in the case of hybrid nanofluid) and 0.04721 (in the case of nanofluid) when activation energy (E) takes an input in the range $0 \leq E \leq 5$.
- Entropy generation rises as the Brinkmann number rises. As the magnetic field parameter increases, there is a corresponding decrease in the fluid's velocity.
- The Bejan number falls as the Brinkmann number and magnetic field increase.

Author Contributions: Conceptualization, B.L. and N.A.S.; methodology, J.G.K. and M.J.B.; software, C.S.R.; validation, B.L. and N.A.S.; formal analysis, C.S.R.; investigation, C.S.R. and P.J.; resources, J.G.K. and M.J.B.; writing—original draft preparation, C.S.R. and P.J.; writing—review and editing, B.L., J.G.K., M.J.B. and N.A.S.; Project administration, C.S.R. and N.A.S.; funding, P.J. All authors have read and agreed to the published version of the manuscript.

Funding: This research received no external funding.

Institutional Review Board Statement: Not Applicable.

Informed Consent Statement: Not Applicable.

Data Availability Statement: The numerical data used to support the findings of this study are included within the article.

Acknowledgments: This research received funding support from the NSRF via the Program Management Unit for Human Resources & Institutional Development, Research and Innovation.

Conflicts of Interest: The authors declare no conflict of interest.

Nomenclature

μ	Dynamic viscosity of the fluid $\left[\text{kg m}^{-1}\text{s}^{-1}\right]$
Sc	Schmidt number
ρ	The density of the fluid $\left[\text{kgm}^{-3}\right]$
Pr	Prandtl number
β_T	Thermal expansion coefficient
$k*$	Mean absorption coefficient
g	Acceleration of gravity
v	Kinematic viscosity $\left[\text{m}^2\text{s}^{-1}\right]$
k_f	Thermal conductivity $\left[\text{Wm}^{-1}\text{K}^{-1}\right]$
f'	Dimensionless velocity
C_p	Heat capacity
u, v	Velocity components in x, y directions $\left[\text{ms}^{-1}\right]$
E	Activation energy parameter
$\delta*$	Nonlinear thermal convection parameter
Re	Suction/injection parameter
η	Similarity variable
R	Radiation parameter
$\sigma*$	Stefan-Boltzmann constant
Gt	Thermal Grashoff number
Gd	Diffusion Grashoff number
ζ	Buoyancy ratio parameter
D_m	Molecular diffusivity $\left[\text{m}^2\text{s}^{-1}\right]$
M	Magnetic field Parameter
Q_0	Volumetric rate of heat source parameter
k_1	Boltzmann constant
E_0	Dimensional activation energy Parameter
Q	Heat source parameter
β_C	Diffusion expansion coefficient
θ	Non-dimensional temperature
m	Fitted rate constant
γ	Reaction rate constant
δ	Temperature difference parameter
λ	Mixed convection parameter
Subscripts	
f	fluid
nf	Nanofluid
hnf	Binary hybrid nanofluid

References

1. Choi, S.U.; Eastman, J.A. *Enhancing Thermal Conductivity of Fluids with Nanoparticles*; No. ANL/MSD/CP-84938; CONF-951135-29; Argonne National Lab. (ANL): Argonne, IL, USA, 1995.
2. Moraveji, A.; Toghraie, D. Computational fluid dynamics simulation of heat transfer and fluid flow characteristics in a vortex tube by considering the various parameters. *Int. J. Heat Mass Transf.* **2017**, *113*, 432–443. [CrossRef]
3. Kavusi, H.; Toghraie, D. A comprehensive study of the performance of a heat pipe by using of various nanofluids. *Adv. Powder Technol.* **2017**, *28*, 3074–3084. [CrossRef]
4. Mostafazadeh, A.; Toghraie, D.; Mashayekhi, R.; Akbari, O.A. Effect of radiation on laminar natural convection of nanofluid in a vertical channel with single-and two-phase approaches. *J. Therm. Anal. Calorim.* **2019**, *138*, 779–794. [CrossRef]
5. Thameem Basha, H.; Sivaraj, R.; Subramanyam Reddy, A.; Chamkha, A.J. SWCNH/diamond-ethylene glycol nanofluid flow over a wedge, plate and stagnation point with induced magnetic field and nonlinear radiation–solar energy application. *Eur. Phys. J. Spec. Top.* **2019**, *228*, 2531–2551. [CrossRef]
6. Alazwari, M.A.; Abu-Hamdeh, N.H.; Goodarzi, M. Entropy optimization of first-grade viscoelastic nanofluid flow over a stretching sheet by using classical Keller-box scheme. *Mathematics* **2021**, *9*, 2563. [CrossRef]
7. Abu-Hamdeh, N.H.; Alsulami, R.A.; Rawa, M.J.; Alazwari, M.A.; Goodarzi, M.; Safaei, M.R. A Significant Solar Energy Note on Powell-Eyring Nanofluid with Thermal Jump Conditions: Implementing Cattaneo-Christov Heat Flux Model. *Mathematics* **2021**, *9*, 2669. [CrossRef]
8. Sabu, A.S.; Wakif, A.; Areekara, S.; Mathew, A.; Shah, N.A. Significance of nanoparticles' shape and thermo-hydrodynamic slip constraints on MHD alumina-water nanoliquid flows over a rotating heated disk: The passive control approach. *Int. Commun. Heat Mass Tran.* **2021**, *129*, 105711. [CrossRef]
9. Dawar, A.; Wakif, A.; Thumma, T.; Shah, N.A. Towards a new MHD non-homogeneous convective nanofluid flow model for simulating a rotating inclined thin layer of sodium alginate-based Iron oxide exposed to incident solar energy. *Int. Commun. Heat Mass Tran.* **2022**, *130*, 105800. [CrossRef]
10. Balla, H.H.; Abdullah, S.; MohdFaizal, W.; Zulkifli, R.; Sopian, K. Numerical study of the enhancement of heat transfer for hybrid CuO-Cu nanofluids flowing in a circular pipe. *J. Oleo Sci.* **2013**, *62*, 533–539. [CrossRef]
11. Iqbal, Z.; Azhar, E.; Maraj, E.N. Utilization of the computational technique to improve the thermophysical performance in the transportation of an electrically conducting Al2O3-Ag/H2O hybrid nanofluid. *Eur. Phys. J. Plus* **2017**, *132*, 1–13. [CrossRef]
12. Mehryan, S.A.; Kashkooli, F.M.; Ghalambaz, M.; Chamkha, A.J. Free convection of hybrid Al2O3-Cu water nanofluid in a differentially heated porous cavity. *Adv. Powder Technol.* **2017**, *28*, 2295–2305. [CrossRef]
13. Mashayekhi, R.; Khodabandeh, E.; Akbari, O.A.; Toghraie, D.; Bahiraei, M.; Gholami, M. CFD analysis of thermal and hydrodynamic characteristics of hybrid nanofluid in a new designed sinusoidal double-layered microchannel heat sink. *J. Therm. Anal. Calorim.* **2018**, *134*, 2305–2315. [CrossRef]
14. Ruhani, B.; Barnoon, P.; Toghraie, D. Statistical investigation for developing a new model for rheological behavior of Silica–ethylene glycol/Water hybrid Newtonian nanofluid using experimental data. *Phys. A Stat. Mech. Its Appl.* **2019**, *525*, 616–627. [CrossRef]
15. Mabood, F.; Yusuf, T.A.; Khan, W.A. Cu–Al_2O_3–H_2O hybrid nanofluid flow with melting heat transfer, irreversibility analysis and nonlinear thermal radiation. *J. Therm. Anal. Calorim.* **2021**, *143*, 973–984. [CrossRef]
16. Mousavi, S.M.; Rostami, M.N.; Yousefi, M.; Dinarvand, S.; Pop, I.; Sheremet, M.A. Dual solutions for Casson hybrid nanofluid flow due to a stretching/shrinking sheet: A new combination of theoretical and experimental models. *Chin. J. Phys.* **2021**, *71*, 574–588. [CrossRef]
17. Raju SS, K.; Babu, M.J.; Raju CS, K. Irreversibility analysis in hybrid nanofluid flow between two rotating disks with activation energy and cross-diffusion effects. *Chin. J. Phys.* **2021**, *72*, 499–529. [CrossRef]
18. Mahesh, A.; Varma SV, K.; Raju CS, K.; Babu, M.J.; Vajravelu, K.; Al-Kouz, W. Significance of non-Fourier heat flux and radiation on PEG–Water based hybrid Nanofluid flow among revolving disks with chemical reaction and entropy generation optimization. *Int. Commun. Heat Mass Transf.* **2021**, *127*, 105572. [CrossRef]
19. Abu Bakar, S.; Md Arifin, N.; Khashi'ie, N.S.; Bachok, N. Hybrid nanofluid flow over a permeable shrinking sheet embedded in a porous medium with radiation and slip impacts. *Mathematics* **2021**, *9*, 878. [CrossRef]
20. Anuar, N.S.; Bachok, N.; Pop, I. Numerical computation of dusty hybrid nanofluid flow and heat transfer over a deformable sheet with slip effect. *Mathematics* **2021**, *9*, 643. [CrossRef]
21. Zainal, N.A.; Nazar, R.; Naganthran, K.; Pop, I. Magnetic Impact on the Unsteady Separated Stagnation-Point Flow of Hybrid Nanofluid with Viscous Dissipation and Joule Heating. *Mathematics* **2022**, *10*, 2356. [CrossRef]
22. Mohd Sohut NF, H.; Soid, S.K.; Abu Bakar, S.; Ishak, A. Unsteady Three-Dimensional Flow in a Rotating Hybrid Nanofluid over a Stretching Sheet. *Mathematics* **2022**, *10*, 348. [CrossRef]
23. Ramesh, G.K.; Madhukesh, J.K.; Das, R.; Shah, N.A.; Yook, S.J. Thermodynamic activity of a ternary nanofluid flow passing through a permeable slipped surface with heat source and sink. *Waves Random Complex Media* **2022**. [CrossRef]
24. Waini, I.; Ishak, A.; Pop, I. Multiple solutions of the unsteady hybrid nanofluid flow over a rotating disk with stability analysis. *Eur. J. Mech. -B/Fluids* **2022**, *94*, 121–127. [CrossRef]
25. Khan, U.; Waini, I.; Zaib, A.; Ishak, A.; Pop, I. MHD mixed convection hybrid nanofluids flow over a permeable moving inclined flat plate in the presence of thermophoretic and radiative heat flux effects. *Mathematics* **2022**, *10*, 1164. [CrossRef]

26. Chu, Y.M.; Bashir, S.; Ramzan, M.; Malik, M.Y. Model-based comparative study of magnetohydrodynamics unsteady hybrid nanofluid flow between two infinite parallel plates with particle shape effects. *Math. Methods Appl. Sci.* **2022**. [CrossRef]
27. Ashraf, M.Z.; Rehman, S.U.; Farid, S.; Hussein, A.K.; Ali, B.; Shah, N.A.; Weera, W. Insight into Significance of Bioconvection on MHD Tangent Hyperbolic Nanofluid Flow of Irregular Thickness across a Slender Elastic Surface. *Mathematics* **2022**, *10*, 2592. [CrossRef]
28. Zhou, C.; Majdalani, J. Large injection and suction driven channel flows with expanding and contracting walls. In Proceedings of the 15th AIAA Computational Fluid Dynamics Conference, Anaheim, CA, USA, 11–14 June 2001; p. 2713.
29. Raza, J.; Rohni, A.M.; Omar, Z. A note on some solutions of copper-water (Cu-water) nanofluids in a channel with slowly expanding or contracting walls with heat transfer. *Math. Comput. Appl.* **2016**, *21*, 24. [CrossRef]
30. Ahmed, N.; Mohyud-Din, S.T.; Hassan, S.M. Flow and heat transfer of nanofluid in an asymmetric channel with expanding and contracting walls suspended by carbon nanotubes: A numerical investigation. *Aerosp. Sci. Technol.* **2016**, *48*, 53–60. [CrossRef]
31. Saba, F.; Ahmed, N.; Khan, U.; Waheed, A.; Rafiq, M.; Mohyud-Din, S.T. Thermophysical analysis of water based (Cu–Al_2O_3) hybrid nanofluid in an asymmetric channel with dilating/squeezing walls considering different shapes of nanoparticles. *Appl. Sci.* **2018**, *8*, 1549. [CrossRef]
32. Mollamahdi, M.; Abbaszadeh, M.; Sheikhzadeh, G.A. Analytical study of Al_2O_3-Cu/water micropolar hybrid nanofluid in a porous channel with expanding/contracting walls in the presence of magnetic field. *Sci. Iran.* **2018**, *25*, 208–220. [CrossRef]
33. Ali, A.; Ali, Y.; Kumam, P.; Babar, K.; Ahmed, A.; Shah, Z. Flow of a nanofluid and heat transfer in channel with contracting/expanding walls. *IEEE Access* **2019**, *7*, 102427–102436. [CrossRef]
34. Shah, N.A.; Wakif, A.; El-Zahar, E.R.; Ahmad, S.; Yook, S.J. Numerical simulation of a thermally enhanced EMHD flow of a heterogeneous micropolar mixture comprising (60%)-ethylene glycol (EG), (40%)-water (W), and copper oxide nanomaterials (CuO). *Case Stud. Therm. Eng.* **2022**, *35*, 102046. [CrossRef]
35. Sajjan, K.; Shah, N.A.; Ahammad, N.A.; Raju, C.S.K.; Kumar, M.D.; Weera, W. Nonlinear Boussinesq and Rosseland approximations on 3D flow in an interruption of Ternary nanoparticles with various shapes of densities and conductivity properties. *AIMS Math.* **2022**, *7*, 18416–18449. [CrossRef]
36. Sarojamma, G.; Lakshmi, R.V.; Narayana, P.V.; Makinde, O.D. Non linear radiative flow of a micropolar nanofluid through a vertical channel with porous collapsible walls. In *Defect and Diffusion Forum*; Trans Tech Publications Ltd.: Bäch, Switzerland, 2018; Volume 387, pp. 498–509.
37. Al-Kouz, W.; Mahanthesh, B.; Alqarni, M.S.; Thriveni, K. A study of quadratic thermal radiation and quadratic convection on viscoelastic material flow with two different heat source modulations. *Int. Commun. Heat Mass Transf.* **2021**, *126*, 105364. [CrossRef]
38. Irfan, M.; Khan, M.; Khan, W.A.; Ahmad, L. Influence of binary chemical reaction with Arrhenius activation energy in MHD nonlinear radiative flow of unsteady Carreau nanofluid: Dual solutions. *Appl. Phys. A* **2019**, *125*, 1–11. [CrossRef]
39. Jamshed, W.; Aziz, A. Cattaneo–Christov based study of TiO_2-CuO/EG Casson hybrid nanofluid flow over a stretching surface with entropy generation. *Appl. Nanosci.* **2018**, *8*, 685–698. [CrossRef]
40. Dauenhauer, E.C.; Majdalani, J. Exact self-similarity solution of the Navier–Stokes equations for a porous channel with orthogonally moving walls. *Phys. Fluids* **2003**, *15*, 1485–1495. [CrossRef]